PHYSICAL REVIEW B **99**, 174417 (2019)

Molecular diamond lattice antiferromagnet as a Dirac semimetal candidate

Yasuhiro Shimizu,[1] Akihiro Otsuka,[2] Mitsuhiko Maesato,[2] Masahisa Tsuchiizu,[3] Akiko Nakao,[4] Hideki Yamochi,[2]
Takaaki Hiramatsu,[5] Yukihiro Yoshida,[2,5] and Gunzi Saito[5,6]
[1]*Department of Physics, Nagoya University, Furo-cho, Chikusa-ku, Nagoya 464-8602, Japan*
[2]*Division of Chemistry, Graduate School of Science, Kyoto University, Sakyo-ku, Kyoto 606-8502, Japan*
[3]*Department of Physics, Nara Women's University, Kitauoyanishi-machi, Nara 630-8506, Japan*
[4]*Neutron Science and Technology Center, CROSS Tokai, Ibaraki 319-1106, Japan*
[5]*Faculty of Agriculture, Meijo University, Shiogamaguchi 1-501 Tempaku-ku, Nagoya 468-8502, Japan*
[6]*Toyota Physical and Chemical Research Institute, Nagakute 480-1192, Japan*

(Received 27 February 2019; revised manuscript received 29 April 2019; published 20 May 2019)

The ground state of a molecular diamond lattice compound (ET)$Ag_4(CN)_5$ is investigated by magnetization and nuclear magnetic resonance spectroscopy. We found that the material exhibits a Mott-insulating ground state with antiferromagnetic long-range ordering at 102 K. The ordered moment shows weak ferromagnetism with a tiny canting angle. The spin susceptibility is well fitted into the diamond lattice Heisenberg model with a nearest-neighbor exchange coupling of 230 K, indicating the less frustrated interactions. The transition temperature elevates up to $\sim$195 K by applying pressure of 2 GPa, which records the highest temperature among organic molecular magnets. The first-principles band calculation without electron correlations suggests that the system is accessible to a three-dimensional topological semimetal with nodal Dirac lines, which has been anticipated on a half-filling diamond lattice.

DOI: 10.1103/PhysRevB.99.174417

I. INTRODUCTION

A half-filling diamond lattice has recently attracted great interest as an example of a three-dimensional (3D) Dirac semimetal with a linearly crossing band dispersion near the Fermi level [1–4], as is known to be in appealing examples including Na_3Bi and Cd_3As_2 [5,6]. A strong topological insulator emerges in the presence of spin-orbit coupling on the diamond lattice as a 3D analog to graphene [1]. Despite the popular crystal structure, the material with the half-filled band has been known only in a putative material, BiO_2 [3]. In the counterpart insulating system, the frustrated local moment on the diamond lattice has been extensively studied as a spin liquid candidate [7–9]. A typical example is the magnetic spinel (AB_2C_4) with an A-site diamond lattice [10–18], where the properties of the disordered state are under intense debate. A (topological) Mott transition is expected to occur from a spin-disordered phase to a Dirac semimetal phase by tuning the electron correlation [2,7].

Organic molecular compounds have provided the platform for investigating the pressure-tuned Mott transition owing to the soft crystal. The well-studied Mott-Hubbard systems such as κ-$(ET)_2X$ and $Z[Pd(dmit)_2]_2$ possess a quasi-two-dimensional triangular lattice of the molecular dimer unit [19–21]. Most molecular compounds have layered and columnar crystal structures due to anisotropic intermolecular interactions between planar molecules. Thus there are only a few examples of 3D molecular compounds including the diamond lattice, except for inorganic-organic hybrid systems such as Li(TCNE) and $Cu(DCNQI)_2$ [22–24], and no example is known for the half-filling diamond lattice consisting of organic molecules. The material search for 3D molecular compounds would be important for developing high-temperature magnets and superconductors.

We present here the molecular material (ET)$Ag_4(CN)_5$ [25] as a prime example of the 3D diamond lattice. It possesses the extremely high-symmetry crystal structure of the orthorhombic $Fddd$ lattice with the following lattice constants: $a = 13.2150(9)$ Å, $b = 19.4783(13)$ Å, and $c = 19.6506(13)$ Å. Each monovalent ET molecule is surrounded by the honeycomb framework of the closed-shell polyanion $[Ag_4(CN)_5]^-_\infty$ in the bc plane, as shown in Fig. 1(a). This unique packing pattern is distinct from those in typical molecular solids. ET molecules are connected by the symmetry operation $[1/4, \pm 1/4, \mp 1/4]$ to construct a diamond lattice with four equivalent nearest neighbor transfers. For the stable monovalence of ET, the system is regarded as a half-filling diamond lattice of the molecular unit [Fig. 1(b)], which can be either a spin-1/2 Heisenberg antiferromagnet or a 3D Dirac semimetal, depending on the strength of electron correlations.

Here we investigate the ground state of the diamond lattice molecular compound (ET)$Ag_4(CN)_5$ through resistivity, magnetization, and nuclear magnetic resonance (NMR) measurements. As expected for the half-filling organics composed of the monovalent ions, the ground state behaves as a Mott insulator with a spin-1/2 on each molecule. We determined the spin structure and the dynamics through the angular dependence of ^{13}C NMR in the antiferromagnetically ordered phase. Together with the band calculation, we discuss the possible Dirac semimetal phase in a weak correlation limit.

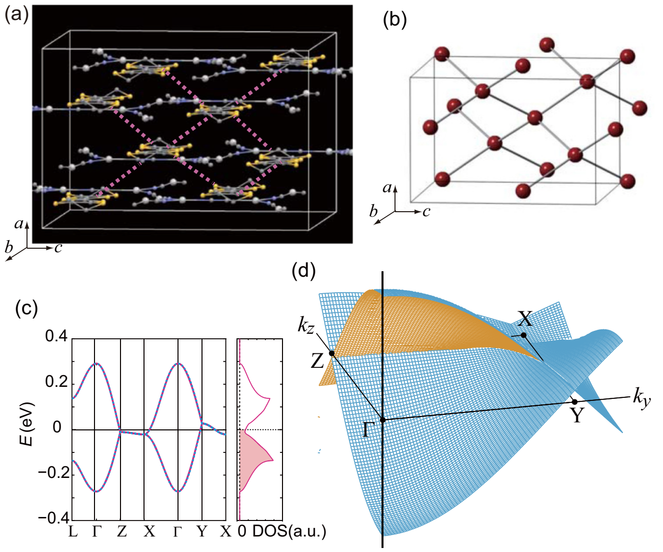

FIG. 1. (a) Crystal structure of $(ET)Ag_4(CN)_5$ with a diamond lattice. Each molecule connected by the symmetry operation [1/4, ±1/4, ∓1/4] has four equivalent nearest-neighbor interactions (dotted lines). (b) Diamond lattice of ET where the red sphere represents the centroid of ET. (c) Highest-occupied molecular orbital (HOMO) bands based on the first-principles calculation. The degenerate band crosses the Fermi level along Z-X-Y due to second neighbor transfers, which gives electron and hole-like Fermi surfaces [Fig. 6(b)]. Dotted lines are the fitting results with tight-binding parameters of transfer integrals (see the Appendix). The density of states (DOS) has the V-shaped energy dependence centered at the Fermi energy. (d) Three-dimensional projection of the band dispersion, showing nodal Dirac lines along the symmetry points along Z-X-Y.

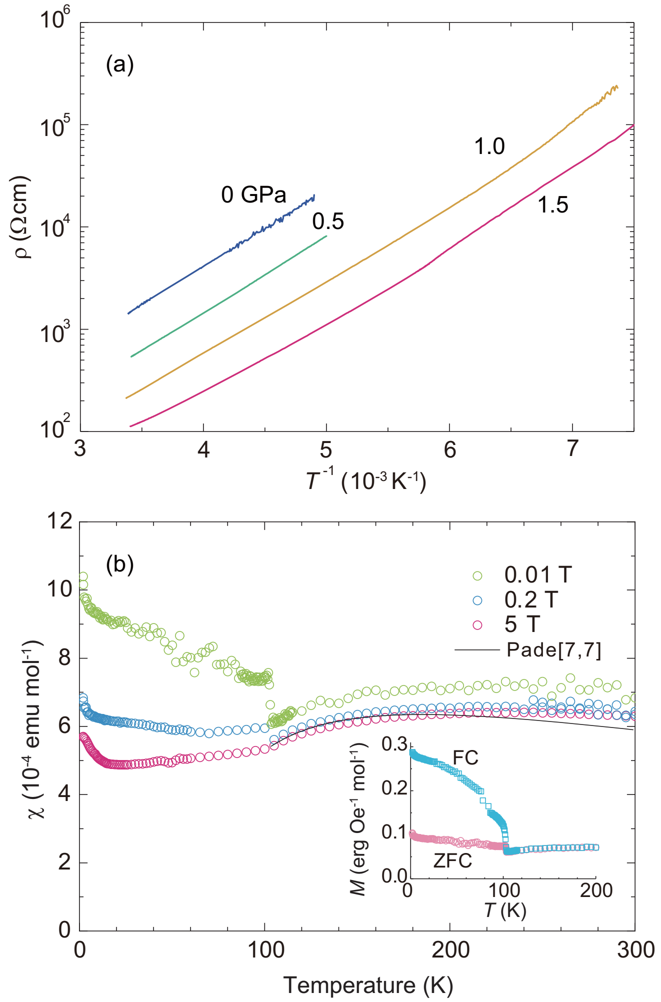

FIG. 2. (a) Inverse temperature dependence of resistivity ρ measured along the b axis of $(ET)Ag_4(CN)_5$ at 0.0, 0.5, 1.0, and 1.5 GPa. (b) Temperature dependence of the magnetic susceptibility χ for zero-field cooling (ZFC) at $H = 0.01$, 0.2, and 5.0 T, where the core diamagnetic contribution was subtracted. The solid curve is a fitting result using a diamond lattice Heisenberg model [31] with the Padé approximant [7, 7] and $J = 230$ K. Inset: ZFC and FC magnetization at 0.01 T.

II. EXPERIMENTAL METHOD

Single crystals of $(ET)Ag_4(CN)_5$ were prepared by galvanostatic electro-oxidation of ET in a 1,1,2-trichloroethane solution of $KAg(CN)_2$ and 18-crown-6 ether. The obtained rhombohedral-shaped crystals of $(ET)Ag_4(CN)_5$ were carefully separated from minor coproducts of κ-$(ET)_2Ag_2(CN)_3$ [26], α'-$(ET)_2Ag(CN)_2$ [27], and κ-$(ET)_2Ag(CN)_2 \cdot H_2O$ [28]. Resistivity was measured with a four-probe dc method at ambient and hydrostatic pressures, where gold wires were attached to a single crystal using the carbon paint. Hydrostatic pressure was applied using a BeCu piston cylinder cell with Daphne 7373 oil and monitored by the Manganin wire resistance. Magnetic susceptibility was measured for a polycrystalline sample by a superconducting quantum interference device magnetometer (Quantum Design MPMS-XL). The core diamagnetism value was calculated as a sum of Pascal's constants (-3.74×10^{-4} emu mol^{-1}). ^{1}H and ^{13}C NMR spectra were obtained for a single crystal in a static magnetic field of 2.0 and 8.5 T, respectively, which were calibrated using the resonance frequency of the standard sample, tetramethylsilane.

III. RESULTS AND DISCUSSION

The band structure of $(ET)Ag_4(CN)_5$ was obtained from the first-principles density functional theory calculation based on the generalized gradient approximation with the WIEN2K code, as shown in Fig. 1(c). Here the band structure was evaluated without considering the anion having the orientational CN/NC disorder. The Fermi energy is located at the half-filling position, where two HOMO bands cross. The two bands are degenerate along the Z-X and Y-X directions, which is characteristic of the diamond lattice [29]. The result qualitatively agrees with the extended Hückel and the tight-binding calculation [25,30]. Along the symmetry positions of the band, nodal Dirac lines appear near the Fermi level, as shown in Fig. 1(d), consistent with the result for the cubic diamond lattice [3].

Despite the semimetallic band structure, the resistivity ρ exhibits insulating temperature (T) dependence, as shown in Fig. 2(a). The activation energy is obtained as $E_b = 0.15$ eV along the b axis at ambient pressure. Together with the paramagnetic spin susceptibility χ [Fig. 2(b)], the system is

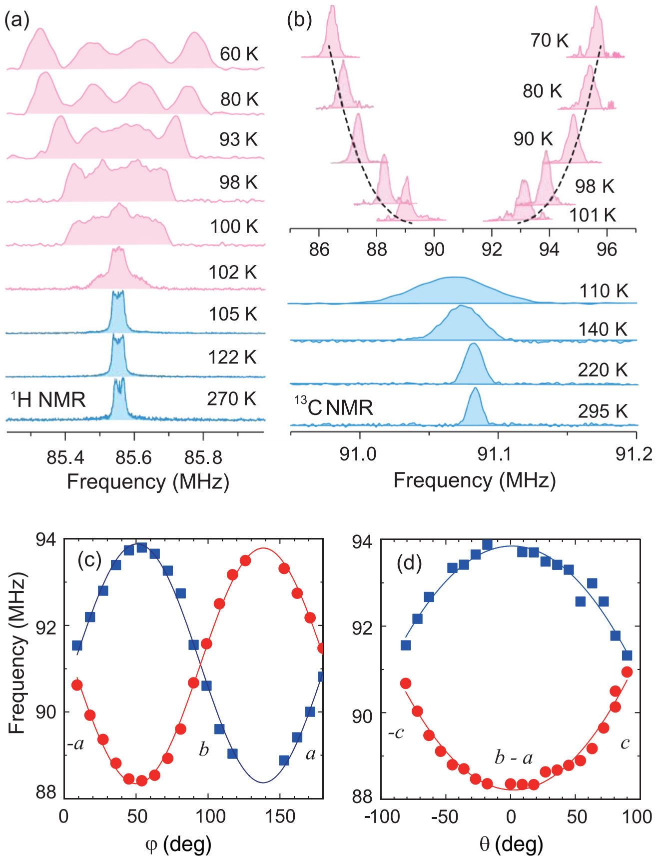

FIG. 3. (a) ^{1}H NMR spectrum along the a axis at 2.0 T. (b) ^{13}C NMR spectrum at 8.5 T applied along [110] corresponding to the magic angle where the ^{13}C-^{13}C dipole coupling vanishes for $T > T_N$. Dotted curves represent temperature dependence of order parameters with the critical exponent $\beta = 0.36$, as expected in 3D Heisenberg antiferromagnets. The vertical axis scales to temperature. (c, d) Angle dependence of ^{13}C NMR frequency in the ordered state at 95 K, where φ and θ are defined by the angles measured from the $-a$ and $-a + b$ directions toward the b and c axes, respectively.

regarded as a Mott insulator arising from the on-site Coulomb interaction U (∼1 eV for the monovalent ET) greater than the bandwidth ($W \sim 0.57$ eV) [Fig. 1(c)]. By applying hydrostatic pressure, ρ is suppressed by an order of magnitude, and E_b decreases to 0.12 eV at 1.5 GPa. An extrapolation to $E_b = 0$ yields a crude estimate of the critical pressure of ∼8 GPa.

The temperature dependence of χ [Fig. 2(b)] is distinct from the Curie-Weiss law in classical paramagnets, but exhibits a broad maximum around 220 K. The weak temperature dependence of χ is similar to a triangular-lattice anitiferromagnet, such as κ-(ET)$_2$Cu$_2$(CN)$_3$ [19], and a 1D Heisenberg antiferromagnet, such as Sr$_2$CuO$_3$ [32], suggesting significant quantum fluctuations. The experimental data are well fitted by the high-temperature series expansion of the $S = 1/2$ diamond lattice Heisenberg model with the Padé approximant [7, 7] [31], yielding the antiferromagnetic exchange coupling $J = 230 \pm 10$ K. An indication of the magnetic transition is observed at $T_N = 102$ K, where χ shows an abrupt increase at low fields. The prominent magnetic field (H) dependence in the magnetization M and the thermal hysteresis [Fig. 2(b)

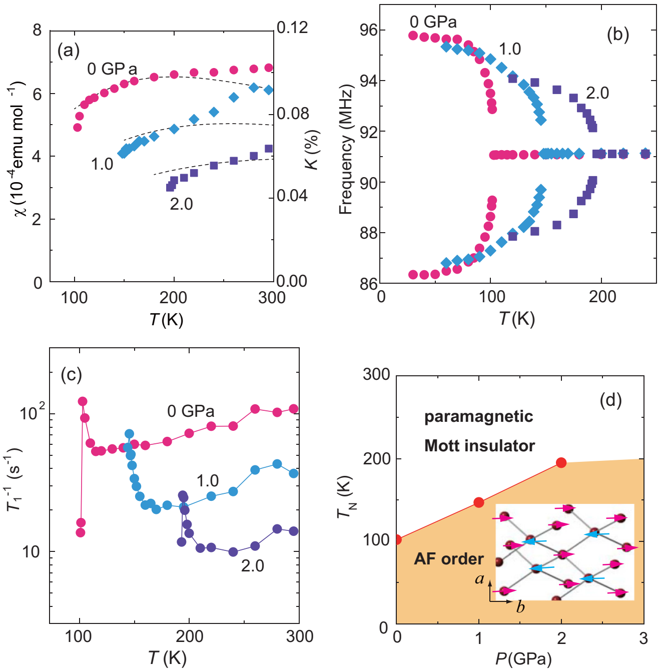

FIG. 4. (a) Static spin susceptibility χ obtained from ^{13}C Knight shift $K = A\chi/(N\mu_B)$ with the hyperfine coupling constant $A = 0.83\text{T}/\mu_B$ determined at 0 GPa. The magnetic field was applied parallel to [110]. Solid curves are the series expansion of the diamond lattice Heisenberg model [31]. (b) ^{13}C NMR frequency defined by the spectral peak across T_N at 0, 1.0, and 2.0 GPa, where the magnetic field is applied along [110]. (c) The nuclear spin-lattice relaxation rate T_1^{-1}. The steep increase toward magnetic ordering occurs due to slowing down to spin fluctuations. (d) Pressure-temperature phase diagram of (ET)Ag$_4$(CN)$_5$ based on the NMR measurements. The inset shows the spin configuration determined by ^{13}C NMR.

inset, Fig. 7] highlight weak ferromagnetism due to the canting of antiferromagnetic moments. The canting moment amplitude is evaluated as 5.4×10^{-5} μ_B.

Microscopic evidence for long-range magnetic ordering is given by ^{1}H and ^{13}C NMR measurements on the single crystal of (ET)Ag$_4$(CN)$_5$, as shown in Fig. 3. Above 105 K, the ^{1}H NMR spectrum [Fig. 3(a)] represents the ^{1}H-^{1}H nuclear dipole coupling with the T-independent linewidth (∼50 kHz). The spectrum begins to split into four below 102 K. The splitting develops upon cooling, signaling the emergence of huge local fields parallel and antiparallel to the external field. The presence of two inequivalent ^{1}H sites on an ET molecule further splits each spectrum into two.

To determine the ordered spin texture, the ^{13}C NMR spectrum was measured for the isotope-enriched crystal at the central double-bonded C sites with the high electron density [33]. There is only a single ^{13}C site manifested as a sharp line in the paramagnetic state. The linewidth grows as spin fluctuations slow down toward T_N. Below T_N, the spectrum largely splits into two due to the antiferromagnetic order, consistent with ^{1}H NMR. The angular dependence of the NMR frequency ω around the crystal axes [Figs. 3(c) and 3(d)] shows that the local field $\mathbf{H}_{\text{loc}}$ exhibits a minimum or maximum against the external magnetic field $\mathbf{H}_0$ parallel to

$\mathbf{b} \pm \mathbf{a}$. A rotation of $\mathbf{H}_0$ from $\mathbf{b} - \mathbf{a}$ to $\mathbf{c}$ confirms $\mathbf{H}_{\rm loc} \parallel \mathbf{b} \pm \mathbf{a}$ [Fig. 3(d)].

Here the ^{13}C nuclear spin experiences a sum of the external field $\mathbf{H}_0$ and the spontaneous local field $\mathbf{H}_{\rm loc}$ produced by the magnetic moment $\mathbf{M}_{\rm loc}$: ω is given by $\omega = \gamma_n H_{\rm eff} = \gamma_n(|\mathbf{H}_0 + \mathbf{H}_{\rm loc}|) = \gamma_n\sqrt{H_0^2 + H_n^2 + 2H_0H_n\cos\vartheta}$, where γ_n is the ^{13}C nuclear gyromagnetic ratio (10.7054 MHz/T) and ϑ is the angle between $\mathbf{H}_0$ and $\mathbf{H}_{\rm loc}$. $\mathbf{H}_{\rm loc}$ is given by $\mathsf{A}\mathbf{M}_{\rm loc} = (A_{aa}M_a, A_{bb}M_b, A_{cc}M_c)$ using the hyperfine coupling tensor A with diagonal components $A_{\alpha\alpha} (\alpha = a, b, c)$ and $\mathbf{M}_{\rm loc} = (M_a, M_b, M_c)$. We determined A from the $K - \chi$ plot (Fig. 8) as $(A_{aa}, A_{bb}, A_{cc}) = (-0.21.-0.21, 1.64)$ T/$\mu_{\rm B}$, which yields the isotropic Fermi contact ($\alpha = 0.41$ T/$\mu_{\rm B}$) and the anisotropic dipole hyperfine coupling ($\beta = 0.62$ T/$\mu_{\rm B}$) as expected for the sp_2 orbital [34].

The temperature dependence of the ^{13}C NMR spectrum for $\mathbf{H}_0 \parallel [110]$ [Fig. 3(b)] demonstrates the evolution of the order parameter, following a scaling law of $\sim(T_{\rm N} - T)^\beta$ with the critical exponent $\beta = 0.36 \pm 0.02$ for $T > 70$ K [Fig. 3(b)]. It is in good agreement with $\beta = 0.368$ in the 3D Heisenberg model [35]. By using the obtained A, we determined the magnetic moment $\mathbf{M}_{\rm loc} = (0.114, 0.889, 0.0)\ \mu_{\rm B}$ with the magnitude $|\mathbf{M}_{\rm loc}| = 0.90 \pm 0.02\ \mu_{\rm B}$ ($\mu_{\rm B}$ is the Bohr magneton) at 40 K. Namely, the easy axis of the moment is directed close to the b axis with the collinear configuration, as schematically shown in Fig. 4(d), consistent with the theoretical ground state for the less frustrated diamond lattice [7,8]. The tiny canting of the moment ($\sim$0.012° obtained from the M-H curve, Fig. 7) was not detected within the accuracy of the NMR measurement.

Intermolecular interactions can be sensitively tuned for the soft organic crystal by applying pressure. Figure 4 shows the ^{13}C Knight shift K and the nuclear spin-lattice relaxation rate T_1^{-1} for (ET)Ag$_4$(CN)$_5$ under hydrostatic pressure up to 2 GPa. Here K is converted into the local spin susceptibility χ using the relation $K = A\chi/(N\mu_{\rm B})$ (N is the Avogadro number) with the hyperfine coupling constant A at ambient pressure [Fig. 4(a)], whereas T_1^{-1} measures the dynamical spin susceptibility that scales to J^{-1} at high temperatures: $T_1^{-1} = \sqrt{\frac{\pi}{3}}\frac{A^2\sqrt{S(S+1)}}{\hbar J\sqrt{z}}$ [36]. We obtained $J = 240 \pm 20$ K at 0 GPa, in agreement with that obtained from χ. By applying pressure, χ is suppressed owing to an increase in J. Fitting of χ into the diamond lattice Heisenberg model [31] allows a rough estimate of the exchange coupling: $J = 310 \pm 40$ K at 1.0 GPa and 400 ± 30 K at 2.0 GPa.

Simultaneously, $T_{\rm N}$ obtained from the spectral splitting [Fig. 4(b)] and the sharp T_1^{-1} peak [Fig. 4(c)] elevates as we increase the pressure: $T_{\rm N} = 150$ K at 1.0 GPa and 195 K at 2.0 GPa [Fig. 4(d)]. It corresponds to the highest magnetic transition temperature among molecular materials including the organic charge-transfer salt [34,37], a transition-metal hybrid system such as Au(tmdt)$_2$ ($T_{\rm N} \sim 110$ K) [38], and a C$_{60}$ complex such as (NH$_3$)KRb$_2$C$_{60}$ ($T_{\rm N} = 76$ K) [39]. In contrast to the mean-field theory giving $T_{\rm N} \sim J = \Theta$ (Θ is the Weiss temperature) for the diamond lattice, the experimentally obtained $T_{\rm N}$ is suppressed to the temperature scale of $\sim J/2$. It is consistent with the significant quantum fluctuations in the $S = 1/2$ Heisenberg antiferromagnet [31]. Despite an increase of $T_{\rm N}$, the magnetic moment is suppressed upon increasing pressure [Fig. 4(b)]. The moment contraction is attributable to quantum fluctuations due to the electron itinerancy and a weak spin dimerization.

Theoretically, the diamond lattice involves geometrical frustration due to 12 next-nearest-neighbor interactions J'. An introduction of the small $J' \sim J/8$ can suppress $T_{\rm N}$ and induce a spin liquid state [7,8]. The frustration is released by strong thermal or quantum fluctuations via an order-by-disorder mechanism, where the ground state is determined by an entropical or energetical selection [7,8]. In the present case, however, a tight-binding calculation suggests the negligible $J'/J \sim (t'/t)^2 < 0.004$. Indeed, the obtained $T_{\rm N}/J = 0.46$ at 0 GPa and 0.49 at 2.0 GPa are consistent with the $S = 1/2$ diamond lattice Heisenberg model including only the nearest-neighbor interaction [31]. Furthermore, in the real system, the highly degenerated (sixfold) spin structure on the diamond lattice should be lifted by single-ion anisotropy (spin-orbit coupling) or lattice distortion (spin-phonon coupling), triggering the magnetic order. Whereas the g value is nearly isotropic ($g_a = 2.0026$, $g_b = 2.0157$, and $g_c = 2.0069$) in (ET)Ag$_4$(CN)$_5$, the spin-orbit coupling as well as the spin-phonon coupling, which leads to the Dzyaloshinskii-Moriya interaction, may play a key role in the spin texture. Despite the presence of the structural CN/NC disorder in the anion, analogous to κ-(ET)$_2X_2$(CN)$_3$ (X = Ag, Cu) without magnetic ordering [19,26], the present system with a less frustrated diamond lattice exhibits a high $T_{\rm N}$. It suggests that the disorder potential from the counter ion plays a negligible effect in the magnetic ground state.

Our finding demonstrates the potential of the molecular conductors for three-dimensional and high-transition temperature magnets through the combination of polymeric counterions. The high-$T_{\rm N}$ Mott insulator may host high-$T_{\rm c}$ superconductivity across the Mott transition under high pressure, because the energy scale of the exchange interaction (>400 K) for (ET)Ag$_4$(CN)$_5$ may be greater than the energy scales of the dimer ET salts such as β'-(ET)$_2$ICl$_2$ ($T_{\rm c} = 14.2$ K at 8.2 GPa) [40] and C$_{60}$ complexes such as Cs$_3$C$_{60}$ ($T_{\rm c} = 38$ K) [39,41]. The band calculation implies that the metallic phase under high pressures may be a 3D Dirac semimetal. Although higher-pressure experiments are now under way, the symmetry of the crystal structure is likely lowered above 3 GPa. If the inversion symmetry is broken, the system can be a strong topological insulator [1,3]. The emergence of a possible Dirac semimetal has recently been observed in a single-component molecular conductor under high pressures [42,43].

IV. CONCLUSION

We investigated the ground state for the uniquely high-symmetry organic Mott insulator with a diamond lattice, (ET)Ag$_4$(CN)$_5$, which possesses nodal Dirac lines in the original band structure without electron correlations. Whereas the charge activation energy exceeds 0.1 eV at ambient pressure, the antiferromagnetic exchange interaction reaches $J = 230$ K, and the long-range magnetic order with the weak ferromagnetism occurs at the high temperature of 102 K. Furthermore, the application of hydrostatic pressure enhances the transition temperature up to 195 K, which is highest among the molecular systems and thus anticipated to host the high-T_c superconductivity at higher pressure.

ACKNOWLEDGMENTS

This work was supported by JSPS KAKENHI Grants No. JP16K13836, No. JP17H05151, No. JP16H04012, No. JP16H04139, No. JP26288035, and No. JP23225005.

APPENDIX

1. X-ray diffractions

The crystal structure was determined by x-ray diffraction measurements with a CCD-type diffractometer (Bruker SMART APEX II) using graphite-monochromated Mo$K\alpha$ radiation ($\lambda = 0.71073$ Å). The crystal structures were solved by a direct method and were refined by a full-matrix least-squares method on F^2 using SHELXL-97. All nonhydrogen atoms were refined anisotropically. The positional parameters of the hydrogen atoms were calculated under a fixed C-H bond length of 0.97 Å with sp^3 configuration of the bonding carbon atoms. In the refinement procedure, an isotropic temperature factor 1.2 times the equivalent one for the bonding carbon atom was applied for hydrogen atoms. The low-temperature x-ray diffraction data were taken down to 12 K at the Institute of Molecular Science. The diffuse x-ray scattering measurement was performed on an imaging plate system by using Si double-crystal monochromatized synchrotron radiation ($\lambda = 0.6885$ Å) at BL-8A of PF in KEK (High Energy Accelerator Research Organization). The crystal mounted on a sapphire rod was cooled by a closed-cycle helium refrigerator.

We obtained the crystal data using the following parameters: orthorhombic space group $Fddd$, lattice constants $a = 13.2150(9)$ Å, $b = 19.4783(13)$ Å, and $c = 19.6506(13)$ Å, the unit cell volume $V = 5058.2(6)$ Å^3, the formula unit $Z = 8$, $F(000) = 3592$, 3598 independent reflections, 82 refined parameters, $R = 0.0449$, $wR = 0.0832$ (for all data), and goodness-of-fit = 1.060. The fractional coordinates are listed in Table I.

TABLE I. Fractional coordinates of (ET)Ag$_4$(CN)$_5$ at 300 K. For N2 located on the inversion center, we assume a 1:1 weight of N and C atoms. The numbers in parentheses denote the standard deviations.

Site	Atom	x	y	z
S1	S	0.12099(9)	0.54209(5)	0.05124(5)
S2	S	0.12689(11)	0.39253(5)	0.03580(6)
C1	C	0.1250	0.5895(3)	0.1250
C2	C	0.1243(3)	0.46257(18)	0.0904(2)
C3	C	0.0962(5)	0.3235(2)	0.0926(2)
H3	H	0.0223	0.3259	0.1034
H3A	H	0.1087	0.2791	0.0686
Ag1	Ag	0.10396(5)	0.3750	0.3750
Ag2	Ag	0.1250	0.1250	0.26246(4)
N1	N	0.1215(3)	0.2209(2)	0.3216(2)
N2	N/C	0.1250	0.1250	0.1538(3)
C4	C	0.1164(3)	0.2745(2)	0.3439(2)
C5	C	0.1250	0.1250	0.1538(3)

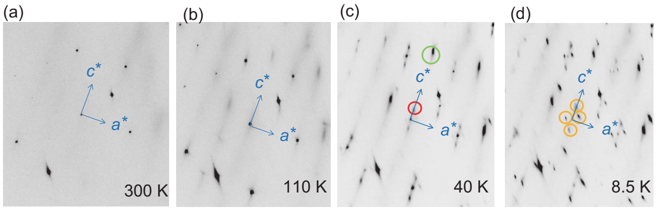

FIG. 5. Diffuse x-ray scattering images for a single crystal of (ET)Ag$_4$(CN)$_5$. The data were taken at 300, 110, 40, and 8.5 K for the ac plane (a^*c^* for the reciprocal lattice). A superstructure develops along the c axis upon cooling.

The weak ferromagnetism below $T_N = 101$ K due to the Dzyaloshinskii-Moriya interaction implies inversion symmetry breaking through a structure distortion. Although we failed to determine the crystal structure at low temperatures, we observed a signature of symmetry lowering in diffuse x-ray scattering peaks (Fig. 5). Below 150 K, the incommensurate superstructure evolves at $(0, 0, \delta)$ ($\delta = 0.45$) along the c axis. The peak becomes clearer but remains incommensurate with decreasing temperature down to 40 K. Then it further splits into four due to an additional superstructure along the a axis at 8.5 K, which corresponds to the symmetry lowering from the orthorhombic to the monoclinic lattice. However, the ^{13}C NMR spectrum does not detect the symmetry breaking, which implies that the superstructure accompanies a tiny distortion or comes from the anion layer.

2. Band structure calculations

The band structure is calculated on the basis of the crystal structure at 300 K. Here we utilized only ET molecules since the orientational CN/NC disorder in the anion gives a technical error of the calculation. To maintain the charge neutrality, the Fermi level is fixed at the half-filling position of the HOMO of the ET molecules. As shown in Fig. 6(a), the HOMO band is well separated from the other band and thus can be regarded as a half-filling single band. The transfer integrals between ET molecules were evaluated

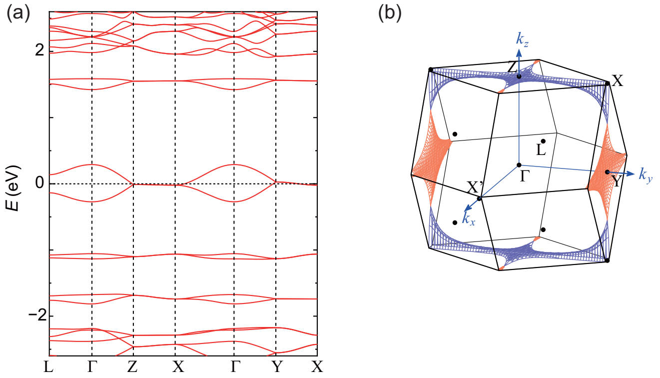

FIG. 6. First-principles band structure calculations. (a) A full band structure of (ET)Ag$_4$(CN)$_5$. The Fermi energy ($E = 0$) is located at the half-filled position of the HOMO band. (b) Electron (blue) and hole (red) Fermi surfaces in the 3D Brillouin zone of the diamond lattice [44].

by fitting the HOMO band into a tight-binding model with six fitting parameters: t_1, t_{2ac}, t_{2ab}, t_3, t_{4a}, and t_{4bc}, where t_1 is the nearest-neighbor transfer integral, t_{2ac} and t_{2ab} are the second-neighbor ones, t_3 is the third-neighbor one, and t_{4a} and t_{4bc} are the fouth-neighbor ones. The fitting yields $t_1 = -68.442$ meV, $t_{2ac} = -0.487$ meV, $t_{2ab} = 4.226$ meV, $t_3 = 1.966$ meV, $t_{4a} = 0.165$ meV, and $t_{4bc} = 1.756$ meV. The transfers other than the nearest-neighbor one give the corrugation of bands at the Fermi level, resulting in the hole and electron Fermi surfaces along the symmetry lines [Fig. 6(b)].

3. Magnetization in the Néel order state

The magnetization M was measured for a randomly orientated polycrystalline sample against the magnetic field H across the antiferromagnetic order temperature T_N. M behaves linearly to H in a paramagnetic state at 150 K and becomes nonlinear to H at low temperatures below T_N (Fig. 7). A hysteresis between the upward and downward H sweeps indicates the spontaneous ferromagnetic moment. From the M-H curve at 1.9 K, the canting angle of antiferromagnetic moments from the easy axis is estimated as less than 0.1° (∼0.012°) at the low-field range.

4. ^{13}C hyperfine coupling tensor

To investigate the spin structure in the ordered state, the ^{13}C hyperfine coupling tensor A is determined from the angular dependence of the Knight shift K around the crystal axis. As shown in Fig. 8, K exhibits a maximum at the a axis corresponding to the Z axis of the Knight-shift tensor K and a minimum at the b and c axes (defined as the X and Y axes, respectively). Since the magnetic susceptibility χ is nearly isotropic for the isotropic g value as observed in the electron paramagnetic resonance, the anisotropic **K** arises from the anisotropic hyperfine coupling **A** due to the anisotropic π orbital on the carbon site.

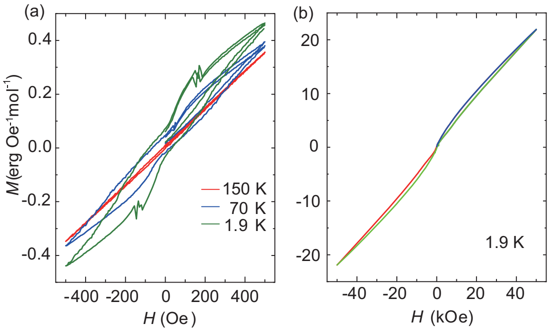

FIG. 7. Magnetization-magnetic field (M-H) curves in (ET)Ag$_4$(CN)$_5$. (a) A low-field cycle between ±500 Oe at different temperatures. An anomaly at 150 Oe and 1.9 K is an extrinsic origin due to the measurement across zero magnetization in raw signals before subtracting the diamagnetic contribution. (b) Magnetic field cycle from −50 to 50 kOe at 1.9 K. A curve starts from zero field and then turns at 50 and −50 kOe.

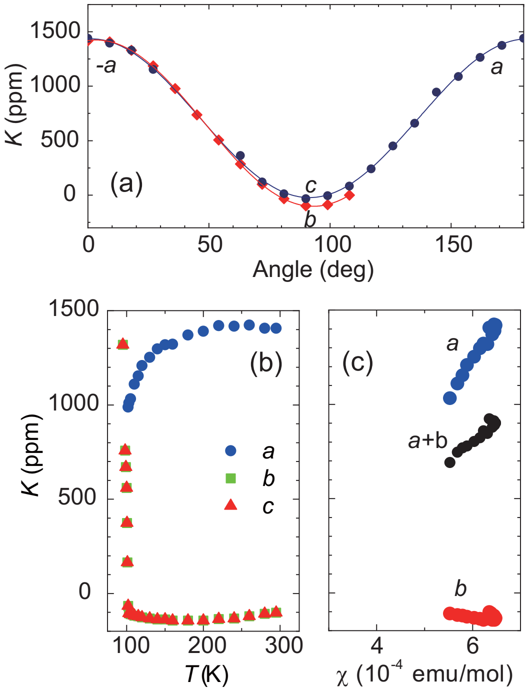

FIG. 8. Angular dependence of ^{13}C NMR spectrum. The data were taken for a single crystal of (ET)Ag$_4$(CN)$_5$ at 8.5 T and 290 K. (b) Temperature dependence of the ^{13}C Knight shift K in (ET)Ag$_4$(CN)$_5$ for $H \parallel a, b$ and c at $H = 8.50$ T. (b) K versus χ plots for the crystal axes, where the linearity coefficient gives the hyperfine coupling constant.

The temperature dependence of K is measured for **H** along the crystal axes (a, b, and c) corresponding to the principal axes (Z, X, and Y) for the local coordinate on the molecule (Fig 8). Although K exhibits weak temperature dependence, we obtained A from linearity coefficients between K and χ for three directions as $\mathsf{A} = (-0.21, -0.21, 1.64)$ T/μ_B. Owing to the uniform stacking of ET molecules without dimerization, the symmetry of the molecular orbital in the crystal holds the directions of the principal axes. The axial symmetry of A ($A_X = A_Y$) indicates the symmetric π orbital with an sp_2 character [34].

[1] L. Fu, C. L. Kane, and E. J. Mele, Phys. Rev. Lett. **98**, 106803 (2007).

[2] Y. Zhang, Y. Ran, and A. Vishwanath, Phys. Rev. B **79**, 245331 (2009).

[3] S. M. Young, S. Zaheer, J. C. Y. Teo, C. L. Kane, E. J. Mele, and A. M. Rappe, Phys. Rev. Lett. **108**, 140405 (2012).

[4] S. Ryu, Phys. Rev. B **79**, 075124 (2009).

[5] Z. K. Liu, Z. K. Liu1, B. Zhou, Z. J. Zhang, Y. Wang, H. M.

Weng, D. Prabhakaran, S.-K. Mo, Z. X. Shen, Z. Fang, X. Dai, Z. Hussain, and Y. L. Chen, Science **343**, 864 (2014).

[6] S. Borisenko, Q. Gibson, D. Evtushinsky, V. Zabolotnyy, B. Büchner, and R. J. Cava, Phys. Rev. Lett. **113**, 027603 (2014).

[7] D. Bergman, J. Alicea, E. Gull, S. Trebst, and L. Balents, Nat. Phys. **3**, 487 (2007).

[8] J.-S. Bernier, M. J. Lawler, and Y. B. Kim, Phys. Rev. Lett. **101**, 047201 (2008).

[9] F. L. Buessen, M. Hering, J. Reuther, and S. Trebst, Phys. Rev. Lett. **120**, 057201 (2018).

[10] V. Fritsch, J. Hemberger, N. Büttgen, E.-W. Scheidt, H.-A. Krug von Nidda, A. Loidl, and V. Tsurkan, Phys. Rev. Lett. **92**, 116401 (2004).

[11] A. Krimmel, H. Mutka, M. M. Koza, V. Tsurkan, and A. Loidl, Phys. Rev. B **79**, 134406 (2009).

[12] K. W. Plumb, J. R. Morey, J. A. Rodriguez-Rivera, H. Wu, A. A. Podlesnyak, T. M. McQueen, and C. L. Broholm, Phys. Rev. X **6**, 041055 (2016).

[13] L. Ge, J. Flynn, J. A. M. Paddison, M. B. Stone, S. Calder, M. A. Subramanian, A. P. Ramirez, and M. Mourigal, Phys. Rev. B **96**, 064413 (2017).

[14] J. R. Chamorro, L. Ge, J. Flynn, M. A. Subramanian, M. Mourigal, and T. M. McQueen, Phys. Rev. Mater. **2**, 034404 (2018).

[15] M. Iakovleva, E. Vavilova, H.-J. Grafe, S. Zimmermann, A. Alfonsov, H. Luetkens, H.-H. Klauss, A. Maljuk, S. Wurmehl, B. Büchner, and V. Kataev, Phys. Rev. B **91**, 144419 (2015).

[16] G. J. MacDougall, A. A. Aczel, Y. Su, W. Schweika, E. Faulhaber, A. Schneidewind, A. D. Christianson, J. L. Zarestky, H. D. Zhou, D. Mandrus, and S. E. Nagler, Phys. Rev. B **94**, 184422 (2016).

[17] G. J. MacDougall, D. Gout, J. L. Zarestky, G. Ehlers, A. Podlesnyak, M. A. McGuire, D. Mandrus, and S. E. Nagler, Proc. Natl. Acad. Sci. USA **108**, 15693 (2011).

[18] O. Zaharko, N. B. Christensen, A. Cervellino, V. Tsurkan, A. Maljuk, U. Stuhr, C. Niedermayer, F. Yokaichiya, D. N. Argyriou, M. Boehm, and A. Loidl, Phys. Rev. B **84**, 094403 (2011).

[19] Y. Shimizu, K. Miyagawa, K. Kanoda, M. Maesato, and G. Saito, Phys. Rev. Lett. **91**, 107001 (2003).

[20] T. Itou, A. Oyamada, S. Maegawa, and R. Kato, Nat. Phys. **6**, 673 (2010).

[21] T. Isono, H. Kamo, A. Ueda, K. Takahashi, M. Kimata, H. Tajima, S. Tsuchiya, T. Terashima, S. Uji, and H. Mori, Phys. Rev. Lett. **112**, 177201 (2014).

[22] C. M. Kareis, S. H. Lapidus, P. W. Stephens, and J. S. Miller, Inorg. Chem. **51**, 3046 (2012).

[23] J.-H. Her, P. W. Stephens, R. A. Davidson, K. S. Min, J. D. Bagnato, K. van Schooten, C. Boehme, and J. S. Miller, J. Am. Chem. Soc. **135**, 18060 (2013).

[24] O. Ermer, Adv. Mater. **3**, 608 (1991).

[25] U. Geiser, H. H. Wang, L. E. Gerdom, M. A. Firestone, L. M. Sowa, and J. M. Williams, J. Am. Chem. Soc. **107**, 8305 (1985).

[26] Y. Shimizu, T. Hiramatsu, M. Maesato, A. Otsuka, H. Yamochi, A. Ono, M. Itoh, M. Yoshida, M. Takigawa, Y. Yoshida, and G. Saito, Phys. Rev. Lett. **117**, 107203 (2016).

[27] M. Beno, M. A. Firestone, P. C. W. Leung, L. M. Sowa, H. H. Wang, and J. M. Williams, Solid State Commun. **57**, 735 (1986).

[28] M. Kurmoo, D. R. Talham, K. L. Pritchard, P. Day, A. M. Stringer, and J. A. K. Howard, Synth. Metals **27**, A177 (1988).

[29] D. J. Chadi and M. L. Cohen, Phys. Status Solidi **68**, 405 (1975).

[30] U. Geiser, H. H. Wang, J. M. Williams, E. L. Venturini, J. F. Kwak, and M.-H. Whangbo, Synth. Met. **19**, 599 (1987).

[31] J. Oitmaa, J. Phys.: Condens. Matter **30**, 155801 (2018).

[32] N. Motoyama, H. Eisaki, and S. Uchida, Phys. Rev. Lett. **76**, 3212 (1996).

[33] J. Larsen and C. Lenoir, Synthesis **1989**, 134 (1989).

[34] K. Miyagawa, K. Kanoda, and A. Kawamoto, Chem. Rev. **104**, 5635 (2004).

[35] H. Benner and J. P. Boucher, in *Magnetic Properties of Layered Transition Metal Compounds*, edited by L. J. de Jonh (Kluwer Academic, Dordrecht, 1990).

[36] T. Moriya, Prog. Theor. Phys. **16**, 23 (1956).

[37] D. F. Smith, C. P. Slichter, J. A. Schlueter, A. M. Kini, and R. G. Daugherty, Phys. Rev. Lett. **93**, 167002 (2004).

[38] Y. Hara, K. Miyagawa, K. Kanoda, M. Shimamura, B. Zhou, A. Kobayashi, and H. Kobayashi, J. Phys. Soc. Jpn. **77**, 053706 (2008).

[39] T. Takenobu, T. Muro, Y. Iwasa, and T. Mitani, Phys. Rev. Lett. **85**, 381 (2000).

[40] H. Taniguchi, M. Miyashita, K. Uchiyama, K. Satoh, N. Mori, H. Okamoto, K. Miyagawa, K. Kanoda, M. Hedo, and Y. Uwatoko, J. Phys. Soc. Jpn. **72**, 468 (2003).

[41] Y. Takabayashi, A. Y. Ganin, P. Jeglic, D. Arcon, T. Takano, Y. Iwasa, Y. Ohishi, M. Takata, N. Takeshita, K. Prassides, and M. J. Rosseinsk, Science **323**, 1585 (2009).

[42] R. Kato, H. Cui, T. Tsumuraya, T. Miyazaki, and Y. Suzumura, J. Am. Chem. Soc. **139**, 1770 (2017).

[43] Z. Liu, H. Wang, Z. F. Wang, J. Yang, and F. Liu, Phys. Rev. B **97**, 155138 (2018).

[44] C. J. Bradley and A. P. Cracknell, *The Mathematical Theory of Symmetry in Solids* (Clarendon, Oxford, 1972).